energies

Article

Thermo-Statistical Investigation of the Solar Air Collector Using Least Angle Regression

Alok Dhaundiyal

Centre for Energy Research, Konkoly Thege M. út 29-33, 1121 Budapest, Hungary; alok.dhaundiyal@ek-cer.hu

Abstract: The paper presents the notion of high dimensionality—in the results—that could change the exergy and energy characteristics of the two-pass solar collector. To examine the energetic aspect of the collector, two different types of absorber plate surfaces were chosen: one that is smooth and one with triangular fins. Both designs have two-pass and wooden baffles underneath their absorber plates. The induced air blower was used for the forced convection of air. To examine the attribute of the data, the least angle regression (LARS) algorithm was used to find a new exergy model without overfitting the data. The second law efficiency dropped by 18.92% for the given models of the solar collector when the air flow rate surged further from 10.10 $g \cdot s^{-1}$ to 12.10 $g \cdot s^{-1}$, whereas the energy efficiency showed contradictory behaviour for the given range of air flow rate. It increased by 3% in the first half of the rise in the air flow rate, and on the other hand, a jump of 8% was recorded in the energy efficiency with a rise in the air flow rate by 19.80%. The addition of wooden baffles in the second passage of the flat plate two-pass collector increased the entropy generation due to air friction by 200%, albeit it dropped by 50% at 12.10 $g \cdot s^{-1}$. Upon increasing the air stream rate from 8.10 $g \cdot s^{-1}$ to 12.10 $g \cdot s^{-1}$, the exergy destruction rate at the front finned surface of the two-pass solar air collector receded by 5.49–8.76%, and at the same time, it elevated for the rear passage provided with the wooden baffles. However, it decreased for both the front and rear surfaces of the solar air collector, as the air flow rate increased by 24.69%.

Keywords: exergy; solar air collector; energy; entropy; regression analysis; air

1. Introduction

The unrestricted emission of greenhouse gases (GHGs), owing to the utilization of fossil fuels has, badly impacted the environment; therefore, it becomes indispensable to replace fossil fuels with eco-friendly ones. According to IEA prediction, the yearly generation rate of renewable power must grow at an average rate of nearly 12% over 2021–2030 to meet the net zero emission target by 2050. Among other sources, the application of renewable energy sources has created a strong grip on the energy market despite the economic slough caused by COVID-19. For instance, in 2020, one-third of total renewable electricity generation was generated by Solar PV and wind, whereas hydro and bioenergy have energy quotas of 25% and 41.66%, respectively. Electricity generation via renewable sources has increased by 7.1%, which is roughly 20% higher than the average annual percentage growth since 2010 [1]. Another facet of renewable energy is in drying crops and preserving perishable agricultural products. In 2016, the estimated value of the global solar thermal collectors, in terms of revenue, was $20.77 billion. It was reported that the Indo-Pacific would be the largest market in terms of revenue. Rapid industrialization across the Indo-Pacific may provide an additional boost to the product demand. However, the extortionate price of the unit would deter production growth for the forecasting period of 2018–2025. The compound annual growth rate (CAGR) of the thermal collector was evaluated to be 8.1% [2]. The gamut of renewable energy is so vast that it should be demarcated by the subject of interest. Here, the attention is focused on the solar air heater and the energetic aspect of

Citation: Dhaundiyal, A. Thermo-Statistical Investigation of the Solar Air Collector Using Least Angle Regression. *Energies* **2023**, *16*, 2461. https://doi.org/10.3390/en16052461

Academic Editor: Carlo Renno

Received: 7 February 2023
Revised: 27 February 2023
Accepted: 2 March 2023
Published: 4 March 2023

the modification performed on it. The rudimentary information about the collector and historical development can be found in the literature [3,4].

The energetic aspect of the flat and trapezoidal plate solar collectors was examined at tilt angles of 15°, 30°, and 45°. It was reported that the increasing tilt, from 15° to 45°, augmented the efficiency of the solar collectors by 38–66%. Relatively, it was noticed that the energy and exergy estimated for the trapezoidal type collector were 8.5% and 8.4%, respectively, higher than that of the flat plate collector. The approach adopted was quantitative, and the effect of entropy generation within different collectors was omitted [5]. In another work, the exergy loss in the flat plate collector was noticed to be highest during noon time, and the corresponding value of airflow rate was recorded to be the lowest (0.0125 $kg \cdot s^{-1}$). While comparing the optimum exergy efficiencies of the solar collectors, it was seen that the staggered collector surpassed the conventional one (flat plate collector) by a huge margin of 77% [6]. Dhaundiyal and Gabremicheal (2021) adopted a different approach-line to examine the exergy of the conventional collector. They performed a component-based exergy investigation to determine the overall availability of solar energy for drying slices of apple. The relative increase in the irreversibility due to carrier fluid was reported to be 30% for the given design [7]. The copper and aluminium-based corrugated absorber plates were used with water as a medium. It was noticed that the increased mass flow rate of water, from 0.0167 $kg \cdot s^{-1}$ to 0.033 $kg \cdot s^{-1}$, led to a rise in the thermal efficiency of both collectors. As compared to the energy and exergy of the aluminium-based collector, the energy and exergy of the copper-based collector were elevated by 38.8% and 15.48%, respectively, when the mass flow rate of water was increased by 49.70% [8]. The two different graphene-based nano-fluids (graphene/acetone and graphene-water) were used in a flat plate collector to examine the exergy of the modified system. It was stated that the exergy efficiency of the thermal collector was relatively increased by 21% when it was compared with the conventional fluid, whereas the entropy generation dropped by 4%. The study was limited to the thermodynamic aspect of the nano-fluid, while the convective properties that are claimed to be enhanced were omitted [9]. A low-temperature organic Rankine cycle (ORC)—based on a flat plate collector—was adopted to determine the energy/exergy characteristics of a new system. The four different working fluids (R245fa, R134a, pentane, and toluene) were used to determine the overall reform in the system. It was claimed that most of the exergy destruction took place at the solar collector, thermal storage tank, and vapour generator. The exergy efficiencies of the solar collector determined for R245fa, R134a, pentane, and toluene were 24.08%, 22.53%, 22.09%, and 21.76%, respectively [10]. In one of the studies, a multi-walled carbon nano tubed water nano-fluid (NF) was used in a solar collector retrofitted with elliptical pipes. The finite volume method was used to solve the three-dimensional conservation equations. It was reported that the application of elliptical pipes in place of circular tubes increased the residence time of fluid, which eventually increased the outlet temperature and exergy of the flat plate solar collector (FPSC). The highest exergy was estimated at a volume fraction of 0.10% [11]. In another study, emphasis was made on the availability of heat energy so that the collector would be able to let it off to a working medium for sufficient time. The artificial neural network (ANN) was used to simulate the experimental solution. The accuracy of the model was reported as 96%. The residual error between ANN and experimental was ±4% [12]. A matrix-based grey model was also proposed to simulate the fluid behaviour of airs inside the flat plate solar collector. While simulating the experimentally determined flow velocity, the absolute percentage error was relatively dropped by 28.49% when the proposed model was compared with the conventional analytical solution [3]. V-type corrugated (DPVCPSAH) and flat surface (DPFPSAH) solar air collectors were investigated. It was reported that the processed air temperature at the outlet of the DPVCPSAH was elevated by 5% when it was tested along with DPFPSAH. Similarly, a 14% jump in the hermos-hydraulic efficiency of the DPVCPSAH was seen as compared to the corresponding value derived for DPFPSAH [13]. A numerical heat transfer model for artificially implanted rectangular ribs was proposed. It was noticed that the velocity distribution reached over

150% of its initial velocity with the increase in the Nusselt number by 66.66%. It was also reported that the geometry of the absorber plate also increased the friction factor. Consequently, it improved the thermal performance of the solar air collector that was experimentally, as well as numerically, examined [14]. Apart from CFD-related models, a theoretical approach based on FORTRAN was adopted to simulate the experimental parameters measured for a flat plate solar collector. However, the residual error was appreciably higher than 10% to forecast the instrumental data [15]. The four different types of surface geometries of absorber plates were examined to compare the solar air collector design in terms of energy and exergy of the system. It was reported that the v-corrugated wire mesh two-pass solar air heater with longitudinal fins shows higher exergy/energy gain than the finned plate two-pass solar air heater with longitudinal fins, roughened plate double-pass solar air heater with longitudinal fins, and conventional flat plate single-pass solar air heater. For all the collectors, energy efficiency increased with the increase in the mass flow rate of air [16]. In another case, the single-pass, double-pass, and triple-pass solar air collectors were examined using the mathematical model. The optimum energy efficiency was derived as the mass flow rate increased with the insignificant rise in air temperature. Conversely, it was noticed that a rise in lower mass flow rate and an increase in air temperature maximized the exergy of the collectors. It was concluded that the energy efficiency of the triple-pass collector surpassed the single-pass and double-pass by 6–14% and 3–6%, respectively [17]. In another study, a numerical simulation method (forced convection model) was used to improve the thermal performance of solar air collectors. The effects of thicknesses (0.4 cm, 0.5 cm, 0.75 cm, 1 cm) of paraffin wax and phase change material (PCM) were evaluated by adding them to the back side of the absorber plate. It was observed, among the other PCM thicknesses, that the PCM layer of 1 cm imparted good transportation of thermal energy, as the operational timing of the unit was stretched by two hours after sunset, whereas the PCM with the highest melting point provided the best thermal performance [18]. Another experimental work used the two-pass solar air collector with multiple curved perforated baffles. The three-dimensional CFD software CFDRC-2008 was used to solve the energy equation for forced convection. It was reported that the maximum thermal efficiency could be obtained if the baffle angle is set at 7°, the hole diameter is 3 mm, and the air flow rate is 0.03 $kg \cdot s^{-1}$ [19]. A mathematical model was developed for a triangular solar air collector. It was claimed that the heat collection capabilities and the solar fraction of a triangular solar air collector with a tilted cover plate at 60° were, respectively, improved by 24.3% and 11.7% when these parameters were compared with the corresponding values derived for the flat plate solar air collector [20].

It was noticed, in an integrated solar heating and cooling system (SHC) with a parabolic trough collector (PTC), that 18.8% of CO_2 emissions could be mitigated using the SHC system at the expense of 21.3% consumption of the primary energy, but the basic energy conservation equations were used to simulate the SHC [21]. In another study, TRNSYS software was used to determine the model for the integrated solar system. The error using the proposed model was noticed to be 7.74% (maximum) and 1.62% (minimum) [22]. The same energy-based equation was used with different trademark. A sun-tracked parabolic trough collector was modelled involving CFD, and it was seen that the residual of 10–4 was encountered in the momentum equation [23]. A mathematical approach was adopted to improve the performance of a vanadium–titanium black ceramic-coated solar collector. An increase in the gross area of the collector reduced the instantaneous collector efficiency by 7.52% [24].

Having undergone literature review [1–22], the software-based research was conducted, which implies the same energy equations were solved again and again using different trademarks. Here, the algorithm or script has been written down and then carried out with regression analysis using the least angle, which was not used in the solar collector before. Therefore, the application-based research has been conducted here.

The objective of this work was to determine the exergy and energy characteristics of the finned and smooth surfaces of the solar air collectors. Alongside this, a linear regression model for the available energy was proposed using the least angle regression (LARS).

2. Materials and Methods

Experimental Details

The two-pass solar air collector with a smooth surface (Collector-I) and the one with the staggered arrangement of the fins (Collector-II) were critically investigated. The air draught was maintained with the induction blowers in Collector-I and II. The second passage in both collectors was provided with the wooden baffles. The schematic diagram of the testing unit is provided in Figure 1.

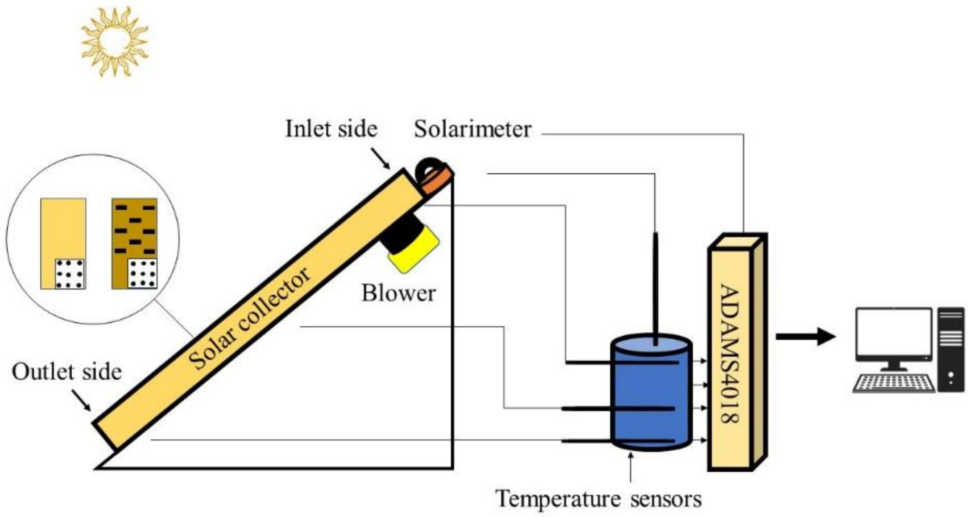

Figure 1. Schematic diagram of the experimental unit.

The volumetric flow rate of a 12-V bilge air blower was 458.73 $m^3 \cdot h^{-1}$. The experimental set-up is illustrated in Figure 2. A bench power supply unit (PSUs) (Voltcraft PS 1440, 0–36 V/DC, 0.01–40 A, and VLP-1602, 2A6V, Hirschau, Germany) was used to power the induction system. The dimensional detail of the collector is provided in Table 1. The electronic data collection was carried out with the support of ADAMS4018 (Advantech, Taipei, Taiwan). Solarimeter, KIMO SL-200 model (Sauermann, Menesterol, France) was considered to calculate the global solar irradiance. The thermocouple type K was considered to measure the temperature of the absorber plate and the air temperature at the inlet and outlet of the collector. At the bottom right side of both collectors, the absorber plate was perforated to provide the passage to the airflow for the second pass. The airspeed was calculated using an anemometer (MS6252A, Peak-meter instruments, Shenzhen, China). The copper material used to make the absorber was of grade C110 quality. Both collectors were facing true south, and the rake angle was kept constant through the working cycle. To increase the absorptivity, the absorber plates of collectors were tinted with the black matt colour. The dimensions of the triangular fins were as follows: the base length is 100 mm, and the height of each fin is 40 mm. A total of 18 fins were rooted on the front surface of Collector-II. The pitch length of the in-line and the thickness of the fins are 200 mm and 1.2 mm, respectively. The air gap between the glazing and absorber plate for the upper pass is 57.50 mm, while it is 35 mm for the lower pass. The expanded polystyrene was used as an insulation material at the back side of the absorber.

(**a**) (**b**)

Figure 2. The experimental set-up of the unit ((**a**) front side, (**b**) rear side).

Table 1. Geometrical dimension of the two-pass solar air collectors.

Components	Dimension (L × W × H)
Wooden frame	12,500 × 500 × 150
Glazing	1218 × 462 × 4
Absorber plate	1218 × 462 × 1.2
Inlet port (*d*)	100
Outlet port (*d*)	100
Insulation	1218 × 462 × 20
Wooden baffle	350 × 20 × 35
Copper fins	100 (*b*) × 1.2 (*t*) × 40

3. Thermo-Statistical Methodology

3.1. Thermodynamics of SAC

The analysis involves thermodynamics and statistical facets of the two-pass solar air collector (SAC). The law of degradation of energy is the basis to measure the exergy/anergy content of the given system. The air used as a working medium is considered incompressible, and the hydrodynamic properties remain altered with the temperature. The physical assessment of SAC is for a steady-state situation. As shown in Equation (1), there is no accumulation of energy in a control volume with time $\left(\frac{dE}{d\tau}\right) = 0$:

$$\left(m_1\left(h_1 + \frac{V_1^2}{2} + Z_1 g\right) + \frac{đQ}{d\tau} - m_2\left(h_2 + \frac{V_2^2}{2} + Z_2 g\right) - \frac{đW}{d\tau}\right)_{V'} = 0 \quad (1)$$

Here, V' denotes the control volume of the system, and the '1' and '2' subscripts represent the inlet and outlet of SAC. m, V, Z, Q, and W represent the air flow rate, enthalpy and velocity of the air stream, datum head of the SAC, as well as heat supply and the network done by the system, respectively.

The entropy generation due to irreversibility in an open system is given by Equation (2):

$$\dot{S_g} = \frac{\partial S}{\partial \tau} - \sum_i \dot{m}_i s_i + \sum_e \dot{m}_e s_e - \frac{\dot{Q}}{T} \quad (2)$$

Here, $\dot{S}_g$ and $\frac{\dot{Q}}{T}$ denote the rate of entropy generation and rate of entropy transfer across the system boundary due to heat.

The rate of entropy growth of the control volume is $\frac{\partial S}{\partial \tau} = 0$, the entropy transfer across the system boundary due to heat transfer rate $(\dot{Q})$, and the entropy transfer in and out of the control volume accompanying mass flow, so the generalized form can be rewritten as:

$$\dot{S_g} = \sum_e \dot{m}_e s_e - \sum_i \dot{m}_i s_i - \frac{\dot{Q}}{T} \quad (3)$$

Here, 'e' and 'i' denote the number of inlets of outlets of the control volumes

The entropy generation, due to the pressure loss in SAC, is given by Equation (4):

$$\dot{S_{g,p}} = -\dot{m}R\left(1 - \frac{\Delta P}{P}\right) \quad (4)$$

The exergy of the system can be derived from the following expression:

$$\psi_1 - \psi_2 = \left[\left(b_1 + \frac{V_1^2}{2} + gZ_1\right) - \left(b_2 + \frac{V_2^2}{2} + gZ_2\right)\right] \quad (5)$$

ψ and b represent exergy and the Kennan function for the air stream.

The second law efficiency for the solar air collectors is estimated from Equation (6):

$$\eta_{II} = \frac{A_{min}}{A} \quad (6)$$

A_{min} represents the minimum exergy intake to perform work, whereas A denotes the actual exergy required to carry out a task.

Likewise, the first law efficiency can be expressed as:

$$\eta_I = \frac{Q_u}{Q_r} \quad (7)$$

Q_u represents the useful heat gain rate by the air (system). Q_r represents the rate of heat transfer from the reservoir.

3.2. *Algorithm of Least Angle Regression*

A basic pictorial representation for two variables (t_1 and t_2) is shown in Figure 3. The optimal direction of the exergy function for an open system was examined by finding the most highly correlated attribute to the target value. If more than one predictor has the same correlation, obtain the average value, and proceed in the same direction (least angle) and at the same angle as the predictors.

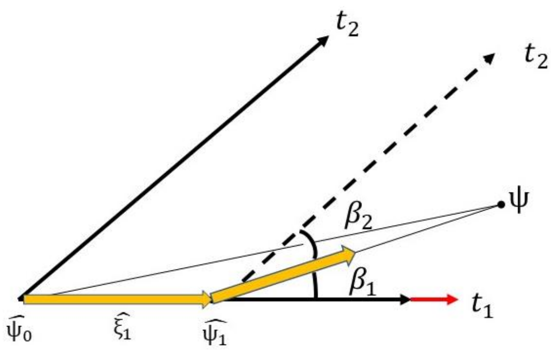

Figure 3. Pictorial illustration of the least angle regression.

Here, $\hat{\psi}_0$ and $\hat{\psi}_1$ are the estimated values of the exergy function, $\hat{\xi}_1$ and $\hat{\xi}_2$ are optimal step sizes, and β_1 and β_2 are the angles formed by variables/predictors with the residual value.

For the least angle regression, a script was prepared in MATLAB 2015b (MathWorks, Natick, MA, USA). The script was based on the following assumptions and steps:

1. The basic procedure to begin the statistical determination of a model is to standardize the predictors (μ = 0 and unit norm).
2. There were no predictors in the model at the beginning of the process.
3. Correlate the predictors with the residual (r) (the difference between the observed value and the estimated response).
4. Once a suitable predictor is correlated with r (geometrically, it implies the least angle with the predictor), keep moving in the same direction until another predictor is not found who is equally correlated with r.
5. Move along in a direction that is equiangular to both predictors.
6. Keep the iterative loop continuous unless all the predictors in a model are not exhausted.

To clarify it further, some mathematical equations are provided.

Suppose, at $\hat{\psi}_0 = 0$, the residual $\psi - \hat{\psi}_0$ is highly correlated to the t_1 variable (least angle), so another response can be written in terms of optimal step size as:

$$\hat{\psi}_1 = \hat{\psi}_0 + \hat{\xi}_1 t_1 \tag{8}$$

Choose optimal step size in such a manner so that the next residual $\psi - \hat{\psi}_1$ is equally correlated to t_1 and t_2. Then, in this case, the point on the bisector is equidistant.

$$\hat{\psi}_2 = \hat{\psi}_1 + \hat{\xi}_2 u_2 \tag{9}$$

If Equation (9) is generalized for k number of predictors, it can be written as:

$$\hat{\psi} = \phi_k \, \Gamma_k + \xi \, \phi_k \, \lambda_k \tag{10}$$

where ϕ_k is a set of those active variables that has a maximal achievable correlation with the residual vector. Γ_k is a set of the coefficient vectors and the directional vectors are denoted by $\lambda_k = \left(\phi_k^T \, \phi_k\right)^{-1} \phi_k^T \, r_k$. In other words, the coefficient vector along the direction of ξ would be $\Gamma_k(\xi) = \Gamma_k + \xi \, \lambda_k$.

Note: The basic energy equations and uncertainty analysis are provided in Supplementary Materials.

4. Results and Discussion

The exergy model of the two-pass collector is derived through the LARS algorithm, and the derived mathematical relationship is represented in tabular form, whereas the empirical data is graphically depicted.

4.1. Thermo-Statistical Behaviour of Two-Pass Collector

The variation of the useful heat gain rate Q_u with the duration is shown in Figure 4. The heat gain rate at the front and rear sections of the two-pass solar air collectors are marked as I-pass and II-pass, respectively. At the constant mass rate, in the I-pass, the average Q_u for collector-II was exceeded by 6.82–9.16% compared to its counterpart collector-I. Similarly, in the II-pass, Q_u in Collector-II was 1.18–18.33% higher than the corresponding value derived for Collector-I. The additional passage (II-pass) improved the overall Q_u by a margin of 4.56–11.59%. The heat gain rate improved by 9.90% as the air flow rate increased by 24.69% in Collector-II, whereas it was 7.54% for Collector-I. The further rise in the air flow rate showed that the heat gain rate in Collector-I was marginally increased by 0.538%, whereas, in the case of Collector-II, it dropped by 3.85% as the air flow rate was increased from 10.10 g·s^{-1} to 12.10 g·s^{-1}, so the effect of air flow rate on the heat gain rate was not the same. However, in both collectors, the heat gain rate increased with the air flow rate, but the rate of increase in Q_u was slowed down with the further change in the air flow rate.

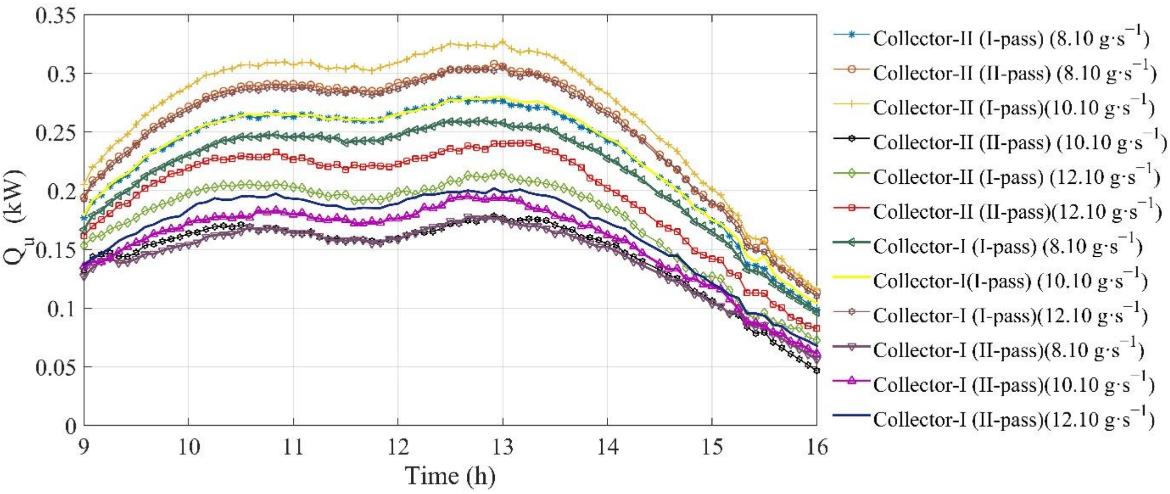

Figure 4. The useful heat gain rate of the air in the two-pass solar collector.

The probability distribution function of Q_u for pass-I was negatively skewed for both Collectors-I and II. A similar pattern was noticed in Q_u for pass-II. The increase in the air flow rate from 8.10 g·s^{-1} to 12.10 g·s^{-1} of air reduced the negative skewness in the probability distribution function of Q_u by the margin of 0.83–1.66% for Collector-I (I-pass). Likewise, in the case of Collector-II (I-pass), it dropped by 3.41–4.06%. That implies the tendency of uniformly distributed heat gain rate increases with the air flow rate, so the air flow rate of 12.10 g·s^{-1} would have a relatively high propensity to provide symmetricity to the useful heat gain of the carrier fluid (air). At 8.10 g·s^{-1}, the skewness in Q_u obtained for Collector-I (I-pass) would be 2.50% higher than that derived for Collector-I (I-pass). As compared to Collector-I (II-pass), it was increased by 15.40% for Collector-II (II-pass) at an air flow rate of 8.10 g·s^{-1}. The distribution functions of *Q*u for the Collector-I and II would share the characteristics of the higher-order Gaussian distribution function. The kurtosis of the distribution function of Q_u also dropped with the increase in the air flow rate, so the existence of an outlier in the calculated value of Q_u would also be reduced. While examining kurtosis (Kr) for Collector-I, the value of Kr was mitigated by 0.60–1.50% and 3.50–3.81% for I-pass and II-pass, respectively, as the air flow rate of air increased from 8.10 g·s^{-1} to 12.10 g·s^{-1}. On the other hand, this margin was widened in the case of Collector-II. It dropped by 4.12–4.72% for I-pass, whereas the reduction in Kr was recorded to be 20–22.82% for II-pass. However, the standard deviation soared up by 8–17% with the increase in the air flow rate for Collector-II (I-pass), which implies that the heat gain rate would drastically vary for both the I-pass and II-pass of Collector-II if the air flow rate increases. A similar pattern was seen for Collector-I, but the magnitude was narrowed down by 0.43% (I-pass) and 7% (II-pass) when the air flow rate changed from 8.10 g·s^{-1} to 10.10 g·s^{-1}. It can be concluded that the overall heat gain was improved by the incorporation of the triangular fins, but perturbation in the heat gain rate was noticed with the increase in the air flow rate. Therefore, a system with the finned surface (Collector-II) would encounter relatively high energy fluctuation at the constant air flow rate, which is not the case with the smooth surface (Collector-I). Comparatively, the useful heat gain for Collector-II (II-pass) was 123.67% higher than that of Collector-I (II-pass), as the air flow rate of air increased by 49.38%. As compared to Collector-I (I-pass), Q_u in Collector-II (I-pass) was merely increased by 1.40% for the same rate of change in the flow rate of the air.

The variation in the exergy gain, $\Delta\psi$ (kJ·kg^{-1}), of the air for the Collector-I and Collector-II is graphically plotted against time in Figure 5. The exergy gain of the air dropped by 34–51.13% as the flow rate of the air in Collector-I (I-pass) increased from 8.10 g·s^{-1} to 12.10 g·s^{-1}, whereas it was 23.25–45.73% for Collector-I (I-pass). A plunge of 18.18–40% occurred due to the rise in the air flow rate of the air in the II-pass of Collector-I, and it was seen to be reduced by 27.11–38.98% for the II-pass of Collector-II. The standard deviation (SD) in $\Delta\psi$ ($kJ \cdot kg^{-1}$) was also reduced with an increase in the air flow rate. It was, respectively, diminished by 38.88–58.33% and 22.58–48.38% for I and II passes of Collector-I. Therefore, apart from the repeatability of the data set, the increase in the air flow rate reduced variability in the exergy of the system with time. Similar statistical behaviour was recorded for both I and II-passes of Collector-II, except for the magnitude, which varies differently. The standard deviation was reduced by 28–50% for the I-pass and 18.18–50% for the II-pass in Collector-II. The distribution functions of $\Delta\psi$ for both Collector-I and Collector-II are negatively skewed, although the skewness in $\Delta\psi$ for Collector-I (I-pass) was 85.71% higher than the corresponding value noted down for Collector-II (I-pass) at 8.10 $g \cdot s^{-1}$. Subsequently, as compared to Collector-II (I-pass), the relative asymmetry in the exergy of Collector-I (I-pass) dwindled by 12.24% at 10.10 $g \cdot s^{-1}$ and 24.13% at 12.12 $g \cdot s^{-1}$. For the II-pass of Collector-I, the skewness was 98.70% lower than the corresponding skewness that occurred in the II-pass of Collector-I at 8.10 $g \cdot s^{-1}$. At the higher air flow rate of the air, the kurtosis value dropped by 4.44% for Collector-I (I-pass) and increased by 23.96% while operating Collector-II (I-pass). Conversely, it stepped up by 27.96% and 51.76% for the II-passes of the Collectors-I and II, respectively. The likelihood of infrequent changes in available energy relatively increases with the air flow rate in Collector-II, and the recurrence of them would be suppressed in Collector-I but only if they both have a single passage. However, the standard deviation decreased for both Collectors-I and II with the increase in the air flow rate. The holistic viewpoint related to the statistical investigations depicted that Collector-I would have relatively low chances to encounter unexpected perturbation in the available energy with time. The maximum change in the exergy of the system (Collector-II) was noticed to be shifted by 1 h 20 min at the constant air flow rate (8.10 $g \cdot s^{-1}$) when it was compared to the corresponding exergy change in Collector-I. No shift in the global maximum value of exergy function was observed in the I-pass of Collector-II at 10.10 $g \cdot s^{-1}$, and a lag of 40 min was estimated in attaining the maximum change in the exergy of Collector-II at 12.10 $g \cdot s^{-1}$. At the same time scale and air flow rate, Collector-I would be more time responsive than Collector-II in terms of exergy gain; nonetheless, the magnitude of the exergy gain in Collector-II (I) was relatively increased by 45% at the same air flow rate (8.10 $g \cdot s^{-1}$).

The change in the average exergy function value for the flow process with the air flow rate of the air is shown in Figure 6. It is clear from Figure 6 that the value of the exergy function will decrease with the increase in the air flow rate of the air. However, the relative change in the exergy function of Collector I and Collector-II might differ quantitatively as well as qualitatively. The exergy drop in both Collectors-I and II varies linearly with the air flow rate of the air. Comparatively, the relative reduction in the exergy was noticed to be relatively higher in Collector-I as the flow rate increased further from 10.10 $g \cdot s^{-1}$ to 12.10 $g \cdot s^{-1}$. At some open air flow rate domains ($9.5 < \dot{m} < 9.6$ and $10.5 < \dot{m} < 11$), the exergy drop would be the same in the II-passes of Collector-I and Collector-II.

The change in the second law efficiency (η_{II}%) with time is illustrated in Figure 7. At 8.10 $g \cdot s^{-1}$, the value of η_{II} for Collector-II (I-pass) was estimated to be 36.16% higher than the corresponding value of η_{II} for Collector-I (I-pass). The maximum relative percentage increase in η_{II} was 46.16% at 12.10 $g \cdot s^{-1}$ for I-pass and 15.83% at 8.10 $g \cdot s^{-1}$ for II-pass of Collector-II (I-pass). Compared to the standard deviation (SD) in the second law efficiency of Collector-I (I-pass), the relative increase in SD for collector-II (I-pass) was 17.61%, 13.39%, and 36.64% at the air flow rates of 8.10 $g \cdot s^{-1}$, 10.10 $g \cdot s^{-1}$, and 12.10 $g \cdot s^{-1}$, respectively. Conversely, in the II-pass of Collector-II, SD only increased at 12.10 $g \cdot s^{-1}$ by the margin of 26.24%, whereas it reduced by 30.47% at 8.10 $g \cdot s^{-1}$ and by 27.16% at 10.10 $g \cdot s^{-1}$. The negative skewness in the η_{II} for Collector-II (I-pass) was reduced by 28.61%, 58.53%, and 52.68% at the corresponding air flow rates of 8.10 $g \cdot s^{-1}$, 10.10 $g \cdot s^{-1}$, and 12.10 $g \cdot s^{-1}$ when the comparison was made with the obtained skewness for Collector-I (I-pass). A similar trend was observed for the second pass of Collector-II (II-pass). The value of Kurtosis for the distribution function of η_{II} varied from 0.39 to 4.09 for the I-pass and 0.31 to 0.44 for the

II-pass of Collector-I. Similarly, it lies in the interval of (−0.17, 4.33) and (0.5, 1.73), while air flows along the I-pass and II-pass of Collector-II. At 12.10 g·s^{-1}, the maximum value of η_{II} for Collector-II with time relatively lagged by 27 min as compared to the Collector-I.

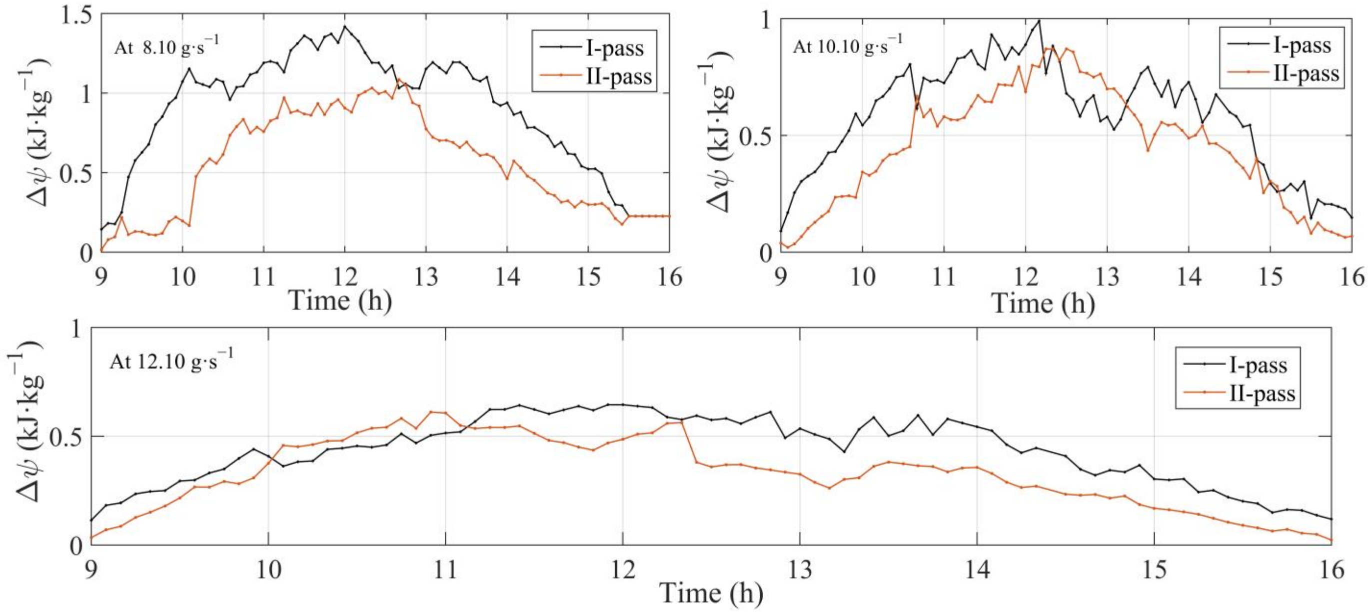

(**a**)

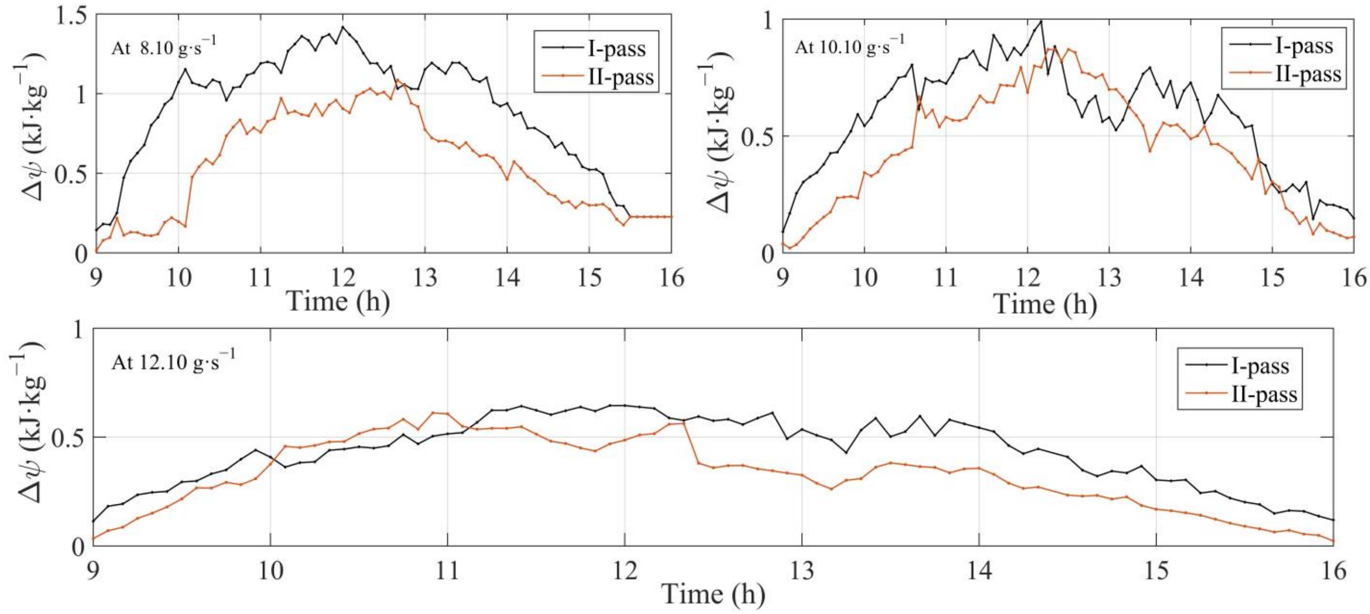

(**b**)

Figure 5. The change in the exergy function ($\Delta\psi$) with time ((**a**) Collector-I, (**b**) Collector-II).

The deviation in the energy efficiency of Collector-I and Collector-II with time is shown in Figure 8. The first law efficiency (η_I) of Collector-II (I-pass) was noticed to be 6.59–7.16% higher than the derived values of η_I for Collector-I (I-pass). The maximum increase in η_I was observed at 10.10 g·s^{-1}. Similarly, the percentage gain in η_I of Collector-II (II-pass), with the increasing air flow rate of the air, varied from 0.64% to 18.31%. The maximum value of η_I derived from Collector-II (I) pass was 8.58% higher than the corresponding value obtained for Collector-I (I pass) at 10.10 g·s^{-1}. Similarly, it surged to 18.05% when it was compared to the maximum η_I of Collector-I (II-pass) at 12.10 g·s^{-1}.

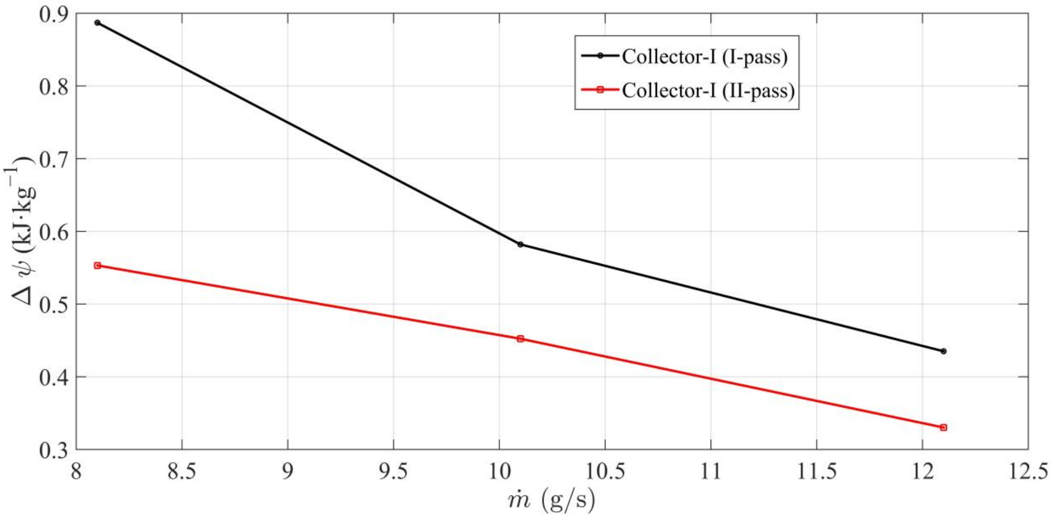

Figure 6. The change in exergy function ($\Delta\psi$) of the system with the air flow rate ($\dot{m}$).

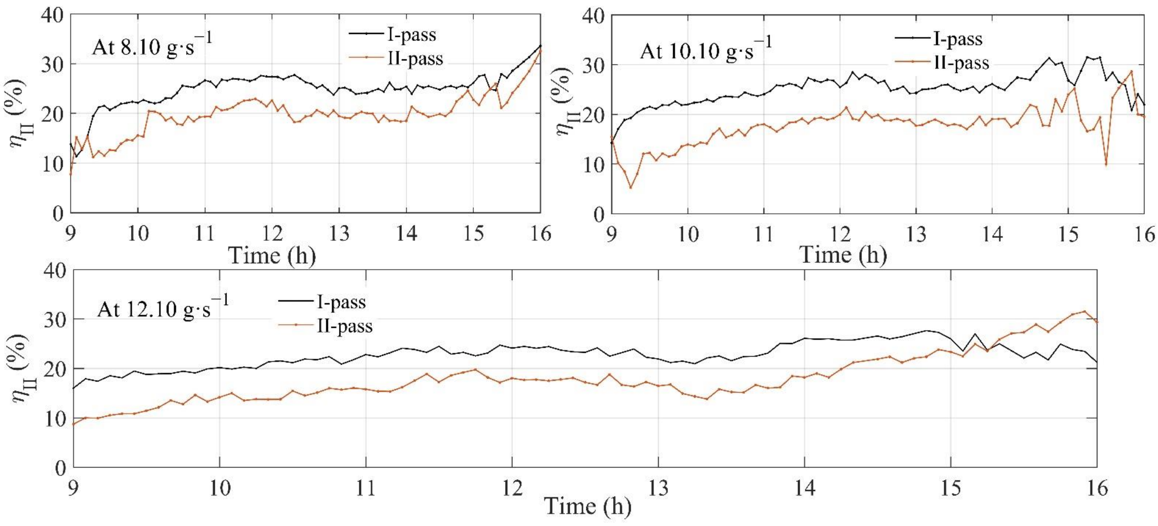

(**a**)

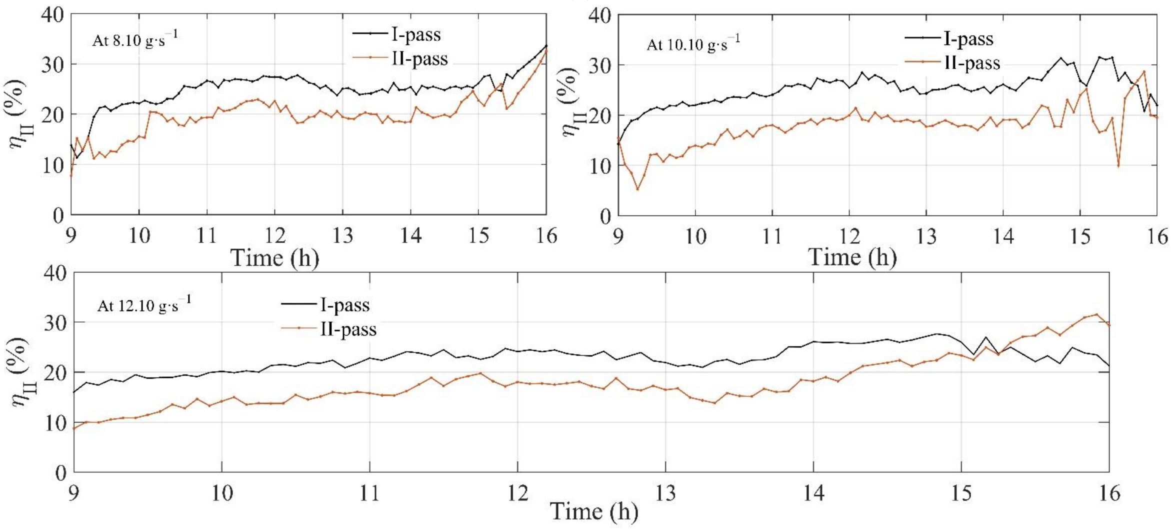

(**b**)

Figure 7. The change in the second law efficiency of the two-pass solar air collector with time ((**a**) Collector-I, (**b**) Collector-II).

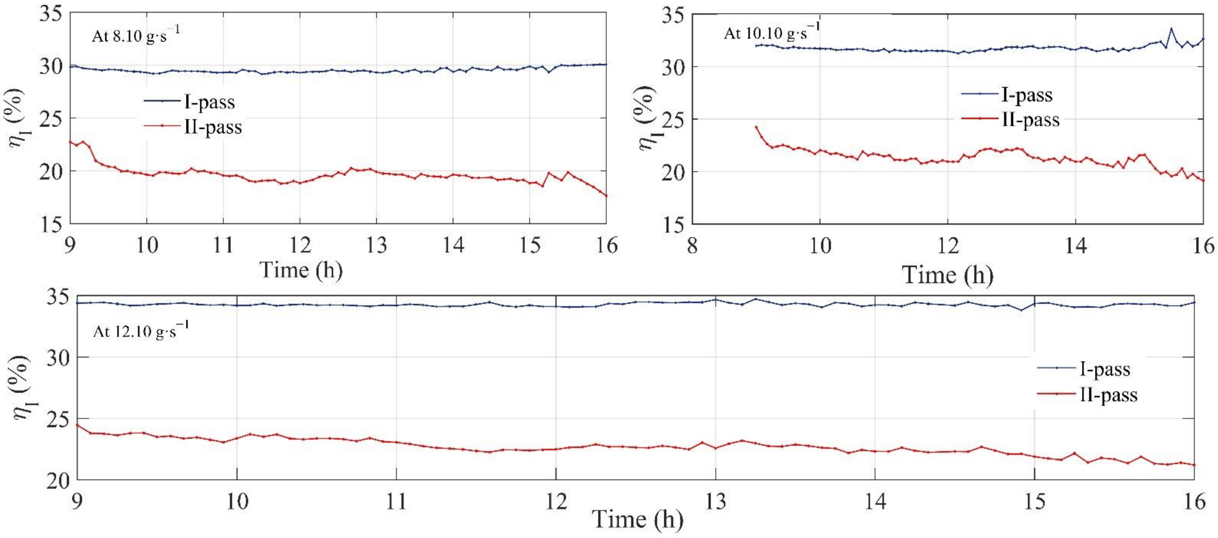

(**a**)

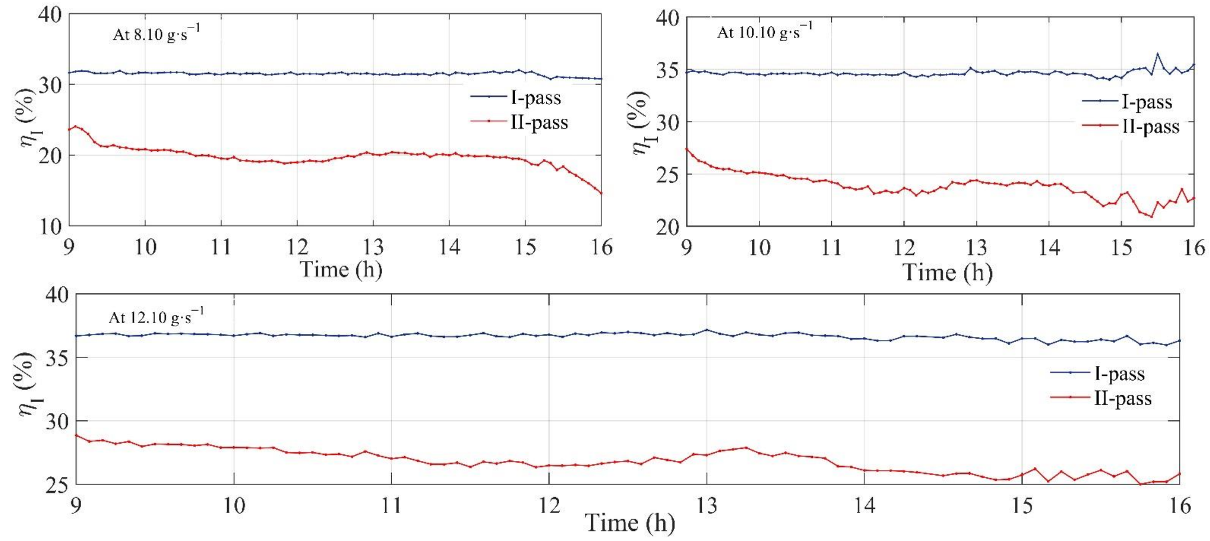

(**b**)

Figure 8. The variation in the first law efficiency, η_I, of the two-pass solar air collector with time ((**a**) Collector-I, (**b**) Collector-II).

A massive jump of 155.88% in η_I was calculated between two passes of Collector-II. Relatively speaking, in terms of energy efficiency, Collector-II fared well with the increasing air flow rate. At the same time, however, the relative deviation around the mean value of the η_I is also magnified by the rise in the air flow rate of the air in the I-pass of Collector-II. It increased by 64.59% and 35.53% in the I-pass and II-pass of Collector-II, respectively. The lowest deviation in the η_I was noted down at 10.10 g·s^{-1} for Collector-II (I-pass). Asymmetry in the distribution function of η_I, for both the I-pass and II-pass of Collector-II, was seen to be negatively skewed at the air flow rates of 10.10 and 12.10 g·s^{-1}. Compared to Collector-II (II-pass), the negative kurtosis in the distribution function of η_I was relatively enhanced by 83.13% for Collector-I (II-pass) at 12.10 g·s^{-1}. At the lower air flow rate, a time lead of 3.6 min in the peak value of η_I was noticed for Collector-II. According to an energy perspective, Collector-II is a bit more promising than its counterpart design, Collector-I. However, variability in η_I would also be relatively high in Collector-II due to higher positive kurtosis and standard deviation.

The effect of the increased air flow rate of the air on the first and second law efficiencies was described graphically in Figure 9. As was seen in Figure 7, the linear characteristic was observed in both η_I and η_{II} efficiencies of the Collector-I and II. The only demarcation is the relative change in the magnitude of η_I and η_{II} efficiencies of the collectors. Undoubtedly, Collector-II surpassed Collector-I in terms of energy efficiency, but the relative change in the first law efficiencies of both collectors were narrowed down with the increasing air flow rate. The effect of air flow rate on the second law efficiency of Collector-II (I-pass) was not as predominant, as it was seen in the case of Collector-I (I-pass). A change of 1.07% in η_{II} against a 24.69% rise in the air flow rate across the Ist-pass of Collector-II was recorded, whereas it amounted to 11.05% for the same surge in the air flow rate across Collector-I (I-pass). Collector-I is more susceptible to the changing air flow rate than Collector-II. At some air flow rates, the second law efficiency of Collector-I (I-pass) marginally exceeded the first law efficiency of Collector-I (II-pass). The positive impact of the second passage on the exergy efficiency of Collector-II was seen only at 12.10 g·s^{-1}, whereas η_I of Collector-I (II-pass) was 8.89% to 33.78% lower than the derived values of η_I for I-pass of Collector-I. In the case of Collector-II, the second passage surpassed the exergy efficiency of the first passage by the margin of 23.51% at an air flow rate of 10.10 g·s^{-1}. The first law efficiency of the II-pass dwindled by 21.10–37.25% when it was compared to η_I of the I-pass of Collector-II.

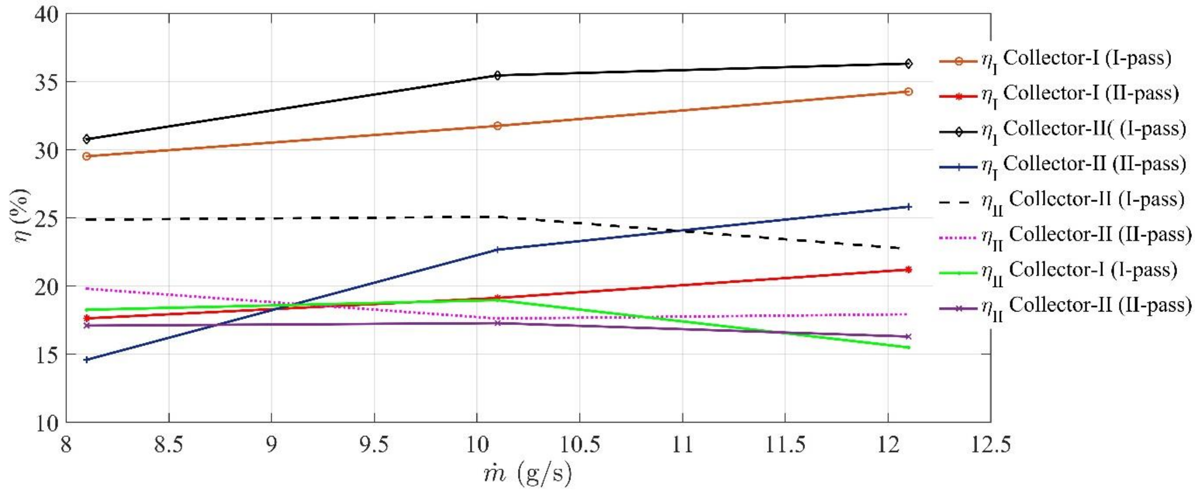

Figure 9. The variation in η_I *and* η_{II} with the air flow rate when flowing across the two parallel ducts.

4.2. Grassmann Diagram of the Two-Pass Air Collector System

The exergy/Grassmann diagram for both collectors is presented in Figure 10. It was seen that the net exergy gain of the air in Collector-I dropped with the increase in the air flow rate from 8.10 g·s^{-1} to 12.10. At 8.10 g·s^{-1}, the net conversion of exergy was 14.71% of the total exergy available to the air at I-pass, whereas the conversion fraction slightly increased to 15.64% when the air flow rate was elevated by 24.69%. The further rise in the air flow rate dropped the exergy gain by 1.10%. However, the average exergy of the air at the inlet of Collector-I might influence the percentage of total available energy (TAH) at the outlet of the two-pass solar air collector. Excluding the exergy of the air at the inlet, the conversion fraction would be increased by a margin of 0.2–1.25%. If the system is examined section-wise, the exergy gains of air in the first passage (I-pass) were 18.53% at an air flow rate of 8.10 g·s^{-1}. Upon comparison with the overall exergy gain of the system, an impressive jump of 5% was noticed in the exergy gain at 8.10 g·s^{-1}, which was estimated to be 4.48% at 10.10 g·s^{-1} and 8.8% at 12.10 g·s^{-1}. The exergy destruction during I-pass and II-pass was remarkably inflated, as the air flow rate varied from 8.10 g·s^{-1} to 12.10 g·s^{-1}. Around 76.50−80.72% of total exergy was discharged to the surrounding area by the open flow system (I-pass). Similarly, it was 61.95–83.56% for the second passage (II-pass). The higher air flow rate will have higher exergy destruction when the flow is between the absorber and the cover plates, whereas it would be the other way around for the air flowing behind the absorber plate. At the mass rate of 8.10 g·s^{-1}, the exergy destruction at II-pass would be 7.06% higher than that obtained for I-pass. However, in the case of 10.10 g·s^{-1} and 12.10 g·s^{-1}, a plunge of 20.19% and 18.77% were, respectively, recorded in the exergy destruction of the air. In a nutshell, it can be concluded that the increasing number of passes would be suitable for the higher flow regime. On the other hand, it is good to have a single-pass system with a lower flow rate if the exergy is the prime concern of interest.

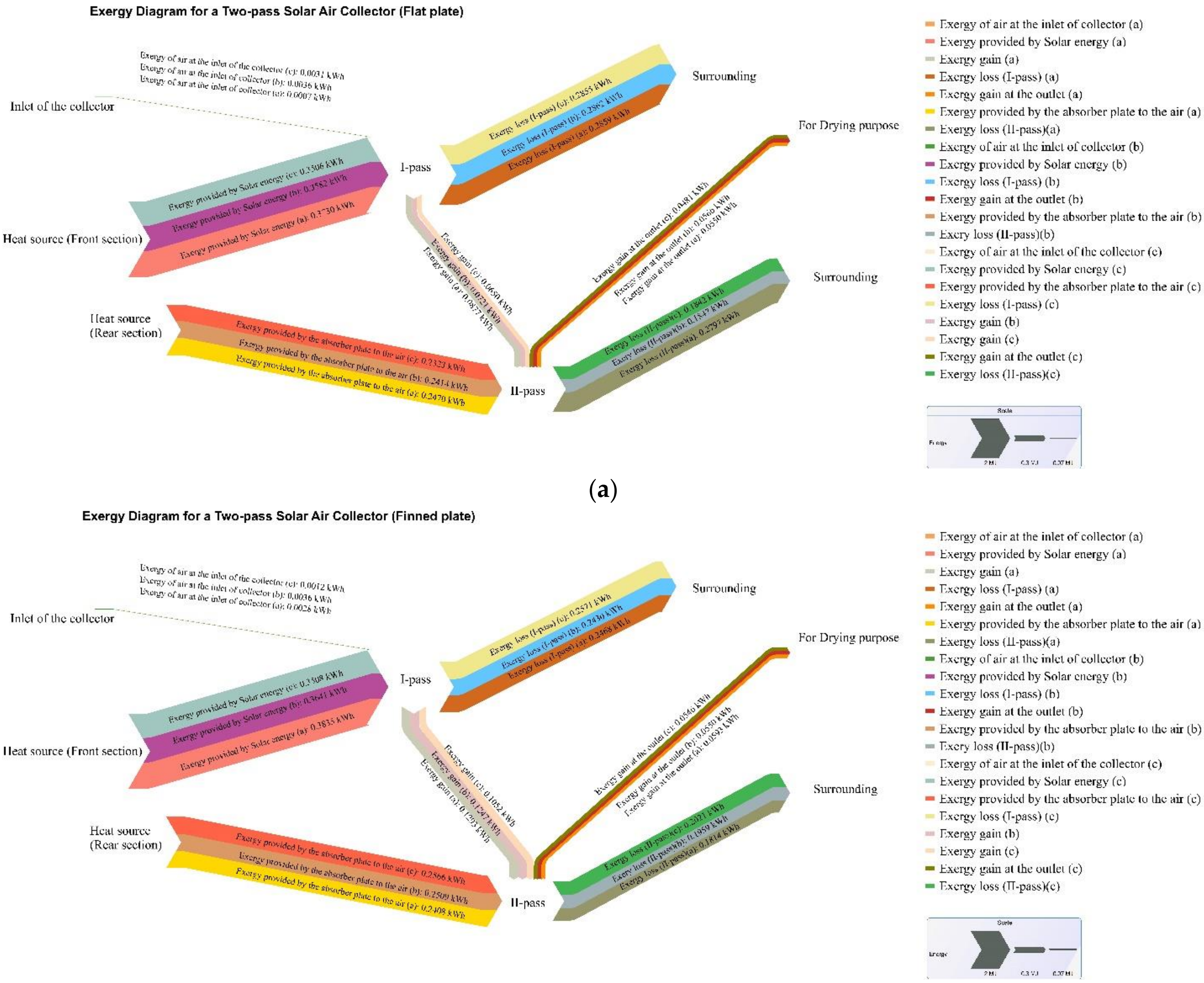

(**a**)

(**b**)

Figure 10. The Grassmann diagram for the two-pass solar air collector ((**a**) Collector-I, (**b**) Collector-II) (a: 8.10 g·s^{-1}, b: 10.10 g·s^{-1}, c: 12.10 g·s^{-1}).

Apart from the smooth surface (Collector-I), an insignificant rise in the overall exergy of the air was noticed for Collector-II with the increase in the air flow rate. The overall exergy gain was elevated by the fraction of 1.04% as the air flow rate increased from 8.10 g·s^{-1} to 12.10 g·s^{-1}. The omission of the initial exergy of the air at the inlet would moderately improve the exergy gain fraction by 0.05–0.11%, which is rather trivial if it is compared with the corresponding rise (0.2–1.25%) in the exergy gain of Collector-I. That implies that the inlet temperature has a relatively low impact on the exergy of Collector-II if the overall exergy gain is pivotal to the examiner. Comparatively, the overall exergy gain of the air in Collector-II surpassed the corresponding gain in Collector-I by 13.12% at the air flow rate of 8.10 g·s^{-1}, although a fall of 4.41% in the exergy gain was pointed out at the air flow of 10.10 g·s^{-1}. If the system is investigated according to the air passage (I and II pass), the exergy gains are 33.55%, 34.24%, and 29.98% of the total exergy (I-pass) provided at the corresponding air flow rates of 8.10 g·s^{-1}, 10.10 g·s^{-1}, and 12.10 g·s^{-1}, which are 43%, 72%, and 63% higher than the exergy gains derived, in parallel, at the same air flow rates for Collector-I. The fractions of exergy destruction at 8.10 g·s^{-1}, 10.10 g·s^{-1}, and 12.10 g·s^{-1} were 63.88%, 66.08%, and 73.04% of the total exergy provided at the inlet (I-pass), as well as 49%, 52.15%, and 55.85% of the total exergy provided at the inlet of II-pass, respectively.

The estimated exergy losses at the constant air flow rate of 8.10 g·s^{-1} in Collector-II were 16.49% (I-pass) and 70.53% (II-pass) lower than that obtained for Collector-I. Succinctly, it can be concluded that the increasing number of passes would be suitable for the higher flow regime. On the other hand, it is good to have a single-pass system with a lower flow rate if the exergy is the prime concern of interest. Conversely, the finned surface with the two passes is relatively good for overall exergy gain in the open flow system with a lower flow rate of the carrier fluid (air), albeit the exergy destruction at a higher air flow rate will limit its application in the high-capacity solar dryers.

The mathematical relationship for the exergy changes and the second and first law efficiencies are, respectively, provided in Tables 2 and 3 for Collector-I and Collector-II. The coefficient values of the polynomial equations are separately compiled in Table 4. It was seen that the higher-order equations fit more closely to the obtained values of exergy gain in Collector-I. The same pattern has been noticed for the other values of $\Delta\psi$ obtained at a higher air flow rate. It implies a higher degree of oscillation, with prevailing time, in the exergy change of the air in Collector-I as compared to Collector-II. Similarly, the polynomial models for other parameters were examined. The polynomial model for the exergy efficiency of Collector-II exhibited higher dimensionality than that of the model derived for Collector-I. However, derived models for energy efficiency with time are uniform in nature and are not skewed significantly with the increase in the air flow rate

Table 2. The mathematical relation of $\Delta\psi$, η_{II} and η_I with time, and t for Collector-I.

Response Variable	$\dot{m}$	Collector-I	Polynomial Model $(p_0t^n + p_1t^{n-1} + p_2t^{n-2} + \ldots)$	RMSE	Adj R^2
$\Delta\psi$	8.10 g·s^{-1}	I-pass	$p_0t^8 + p_1t^7 + p_2t^6 + p_3t^5 + p_4t^4 + p_5t^3 + p_6t^2 + p_7t + p_8$	0.08	0.95
		II-pass	$p_5t^3 + p_6t^2 + p_7t + p_8$	0.07	0.94
	10.10 g·s^{-1}	I-pass	$p_4t^4 + p_5t^3 + p_6t^2 + p_7t + p_8$	0.08	0.86
		II-pass	$p_4t^4 + p_5t^3 + p_6t^2 + p_7t + p_8$	0.02	0.99
	12.10 g·s^{-1}	I-pass	$p_4t^4 + p_5t^3 + p_6t^2 + p_7t + p_8$	0.04	0.93
		II-pass	$p_2t^6 + p_3t^5 + p_4t^4 + p_5t^3 + p_6t^2 + p_7t + p_8$	0.02	0.98
η_{II}	8.10 g·s^{-1}	I-pass	$p_6t^2 + p_7t + p_8$	0.65	0.95
		II-pass	$p_4t^4 + p_5t^3 + p_6t^2 + p_7t + p_8$	0.94	0.97
	10.10 g·s^{-1}	I-pass	$p_5t^3 + p_6t^2 + p_7t + p_8$	0.88	0.89
		II-pass	$p_6t^2 + p_7t + p_8$	0.55	0.98
	12.10 g·s^{-1}	I-pass	$p_5t^3 + p_6t^2 + p_7t + p_8$	1.10	0.62
		II-pass	$p_0t^8 + p_1t^7 + p_2t^6 + p_3t^5 + p_4t^4 + p_5t^3 + p_6t^2 + p_7t + p_8$	0.80	0.95
η_I	8.10 g·s^{-1}	I-pass	$p_5t^3 + p_6t^2 + p_7t + p_8$	0.04	0.95
		II-pass	$p_0t^8 + p_1t^7 + p_2t^6 + p_3t^5 + p_4t^4 + p_5t^3 + p_6t^2 + p_7t + p_8$	0.31	0.86
	10.10 g·s^{-1}	I-pass	$p_3t^5 + p_4t^4 + p_5t^3 + p_6t^2 + p_7t + p_8$	0.12	0.84
		II-pass	$p_4t^4 + p_5t^3 + p_6t^2 + p_7t + p_8$	0.44	0.77
	12.10 g·s^{-1}	I-pass	$p_2t^6 + p_3t^5 + p_4t^4 + p_5t^3 + p_6t^2 + p_7t + p_8$	0.13	0.14
		II-pass	$p_4t^4 + p_5t^3 + p_6t^2 + p_7t + p_8$	0.25	0.86

Table 3. The mathematical relation of $\Delta\psi$ and η_{II} with time, t, and the inlet temperature of the air, respectively, for Collector-II.

Output	$\dot{m}$	Collector-II	Polynomial Model $(p_0t^n + p_1t^{n-1} + p_2t^{n-2} + \ldots)$	RMSE	Adj R^2
$\Delta\psi$	8.10 g·s^{-1}	I-pass	$p_5t^3 + p_6t^2 + p_7t + p_8$	0.07	0.97
		II-pass	$p_5t^3 + p_6t^2 + p_7t + p_8$	0.06	0.92
	10.10 g·s^{-1}	I-pass	$p_5t^3 + p_6t^2 + p_7t + p_8$	0.06	0.96
		II-pass	$p_4t^4 + p_5t^3 + p_6t^2 + p_7t + p_8$	0.04	0.94
	12.10 g·s^{-1}	I-pass	$p_2t^6 + p_3t^5 + p_4t^4 + p_5t^3 + p_6t^2 + p_7t + p_8$	0.03	0.98
		II-pass	$p_6t^2 + p_7t + p_8$	0.01	0.98
η_{II} %	8.10 g·s^{-1}	I-pass	$p_2t^6 + p_3t^5 + p_4t^4 + p_5t^3 + p_6t^2 + p_7t + p_8$	0.11	0.89
		II-pass	$p_2t^6 + p_3t^5 + p_4t^4 + p_5t^3 + p_6t^2 + p_7t + p_8$	0.91	0.94
	10.10 g·s^{-1}	I-pass	$p_3t^5 + p_4t^4 + p_5t^3 + p_6t^2 + p_7t + p_8$	1.47	0.76
		II-pass	$p_3t^5 + p_4t^4 + p_5t^3 + p_6t^2 + p_7t + p_8$	1.28	0.89
	12.10 g·s^{-1}	I-pass	$p_5t^3 + p_6t^2 + p_7t + p_8$	1.44	0.65
		II-pass	$p_5t^3 + p_6t^2 + p_7t + p_8$	1.29	0.93
η_I %	8.10 g·s^{-1}	I-pass	$p_6t^2 + p_7t + p_8$	0.06	0.93
		II-pass	$p_1t^7 + p_2t^6 + p_3t^5 + p_4t^4 + p_5t^3 + p_6t^2 + p_7t + p_8$	0.25	0.96
	10.10 g·s^{-1}	I-pass	$p_6t^2 + p_7t + p_8$	0.08	0.91
		II-pass	$p_1t^7 + p_2t^6 + p_3t^5 + p_4t^4 + p_5t^3 + p_6t^2 + p_7t + p_8$	0.21	0.96
	12.10 g·s^{-1}	I-pass	$p_2t^6 + p_3t^5 + p_4t^4 + p_5t^3 + p_6t^2 + p_7t + p_8$	0.14	0.62
		II-pass	$p_5t^3 + p_6t^2 + p_7t + p_8$	0.46	0.74

The average values of the thermodynamic parameters for Collector-I and Collector-II are tabulated in Tables 5 and 6, respectively. Compared to the corresponding values of η_{II} for Collector-I, the second-law efficiency (η_{II}) for I-pass at 8.10 g·s^{-1}, 10.10 g·s^{-1}, and 12.10 g·s^{-1} was, correspondingly, increased by 35.23%, 32.41%, and 46.92%. Conversely, the relative rise in the second-law efficiency (η_{II}) of Collector-II (II-pass) was noticed only at 8.10 g·s^{-1}, whereas it was dropped by 9.36% and 1.30% at the corresponding air flow rates of 10.10 g·s^{-1} and 12.10 g·s^{-1}. In both Collectors-I and II, the increasing air flow rate led to a reduction in η_{II} of I-pass and II-pass, whereas the first law efficiency (η_I) of Collector-I and Collector-II increases with the surging air flow rate. Compared to the estimated values of η_I for Collector-I, the relative rise in η_I at 8.10 g·s^{-1}, 10.10 g·s^{-1}, and 12.10 g·s^{-1} was 6.57%, 9.10%, and 7.00%, as well as 0.61%, 11.91%, and 18.34% for the I and II-passes of Collector-II, respectively. The estimated exergy destruction rate, I (W), for Collector-II (I-pass) at the air flow rate of 8.10 g·s^{-1} was 16.73% lower than the recorded value of I (W) for the I-pass of Collector-I. Similarly, it dropped by 2.69% when the II-pass of Collector-II was compared with the corresponding pass of Collector-I at the same air flow rate. Relatively speaking, the exergy destruction rate in Collector-II is higher than that of Collector-I, as the air flow rate of the air increases from 8.10 g·s^{-1} to 12.10 g·s^{-1}. The entropy generation, due to the pressure drop in Collector-II, was estimated to be twice the corresponding value derived for Collector-I at 8.10 g·s^{-1}. The enthalpy of the air relatively increased with the rise in the air flow rate across Collector-II (I-pass), but the same effect was not observed in the II-pass of the same collector. A leap of 22.97–31.83% was noticed in the air enthalpy, but a plummet of 11.64–17.48% was also seen at the same time in the II-pass of Collector-II. The useful heat gain by the air in Collector-II (I-pass) was 3%, 17.39%, and 8% higher than the corresponding heat gain obtained by Collector-I (I-pass) at 8.10 g·s^{-1}, 10.10 g·s^{-1}, and 12.10 g·s^{-1}, respectively, albeit there was no change in the heat gain rate of the air flowing across the II-pass of Collector-II. As compared to the useful heat gain rate of the air in Collector-I (II-pass), it was improved by 12.5% at an air flow rate of 10.10 g·s^{-1} and by 17.64% at 12.10 g·s^{-1} in Collector-II (II-pass), which was observed at 10.10 g·s^{-1}. The Keenan function for Collector-II (I-pass) increased by 45.55–66.66%, but it dropped by 2–2.77% as the air flow rate increased from 8.10 g·s^{-1} to 12.10 g·s^{-1}. Qualitatively, the finned surface did not play any pivotal role in the increase in the air flow rate when it was compared to Collector-I. However, some quantitative enhancement was seen in the energy efficiency of the finned collector (Collector-I), but the presence of the second and the exergy loss due to entropy generation increased the irreversibility within the open flow system of Collector-II. There must be an optimum air flow rate to allow both the collector to function properly and the degradation of energy to be minimized to some extent. From this analysis, the air flow rate should be within the range of 8.10–10.10 g·s^{-1} to avoid the degradation of energy for the two-pass open flow system.

Table 4. The coefficient values derived through the LARS algorithm.

Output	$\dot{m}$	Collector Type		p_0	p_1	p_2	p_3	p_4	p_5	p_6	p_7	p_8
$\Delta\psi$	8.10 g·s^{-1}	I	I-pass	0.04	0.03	−0.22	−0.08	0.38	0.07	−0.57	−0.20	1.27
			II-pass	0.00	0.00	0.00	0.00	0.00	0.14	−0.31	−0.25	0.84
		II	I-pass	0.00	0.00	0.00	0.00	0.00	0.16	−0.53	−0.39	1.81
			II-pass	0.00	0.00	0.00	0.00	0.00	0.06	−0.23	−0.14	0.81
	10.10 g·s^{-1}	I	I-pass	0.00	0.00	0.00	0.00	−0.01	0.06	−0.21	−0.17	0.81
			II-pass	0.00	0.00	0.00	0.00	0.05	0.02	−0.39	−0.05	0.74
		II	I-pass	0.00	0.00	0.00	0.00	0.00	0.04	−0.39	−0.11	1.37
			II-pass	0.00	0.00	0.00	0.00	0.02	0.024	−0.24	−0.05	0.64
	12.10 g·s^{-1}	I	I-pass	0.00	0.00	0.00	0.00	0.011	0.014	−0.19	−0.05	0.60
			II-pass	0.00	0.00	0.04	−0.01	−0.24	0.14	0.19	−0.24	0.38
		II	I-pass	0.00	0.00	0.03	0.01	−0.15	−0.04	−0.14	0.004	0.98
			II-pass	0.00	0.00	0.00	0.00	0.00	0.00	−0.12	0.02	0.48
η_{II} %	8.10 g·s^{-1}	I	I-pass	0.00	0.00	0.00	0.00	0.00	0.00	−0.47	11.71	−51.58
			II-pass	0.00	0.00	0.00	0.00	1.67	3.71	−8.26	−3.87	22.51
		II	I-pass	0.00	0.00	−0.10	0.09	0.06	2.52	−1.68	−2.35	26.29
			II-pass	0.00	0.00	1.27	−0.71	−3.98	4.82	1.89	3.04	−20.03
	10.10 g·s^{-1}	I	I-pass	0.00	0.00	0.00	0.00	0.00	1.19	−1.38	−1.64	20.63
			II-pass	0.00	0.00	0.00	0.00	0.00	0.00	−1.30	33.43	−191.5
		II	I-pass	0.00	0.00	0.00	−1.66	−0.91	5.93	1.18	−2.27	25.45
			II-pass	0.00	0.00	0.00	−1.24	0.02	5.13	−1.43	−1.73	18.96
	12.10 g·s^{-1}	I	I-pass	0.00	0.00	0.00	0.00	0.00	0.04	−1.77	23.65	−89.99
			II-pass	−1.42	−0.17	8.53	0.27	−19.36	3.05	15.68	−5.79	15.19
		II	I-pass	0.00	0.00	0.00	0.00	0.00	0.09	−1.26	1.65	24.09
			II-pass	0.00	0.00	0.00	0.00	0.00	0.25	−9.18	111.2	−432.3
η_I%	8.10 g·s^{-1}	I	I-pass	0.00	0.00	0.00	0.00	0.00	−0.002	0.12	−1.98	39.29
			II-pass	−0.11	−0.54	0.73	2.36	−1.32	−3.29	0.82	1.15	19.36
		II	I-pass	0.00	0.00	0.00	0.00	0.00	0.00	−0.07	−0.17	31.47
			II-pass	0.00	−0.64	0.13	2.90	−0.82	−4.86	1.36	2.27	19.41
	10.10 g·s^{-1}	I	I-pass	0.00	0.00	0.00	0.11	0.10	−0.38	−0.07	0.33	31.63
			II-pass	0.00	0.00	0.00	0.00	0.04	−0.50	−0.14	0.22	21.31
		II	I-pass	0.00	0.00	0.00	0.00	0.00	0.00	0.10	0.04	34.51
			II-pass	0.00	−0.40	0.45	2.38	−1.62	−4.68	1.44	1.75	23.57
	12.10 g·s^{-1}	I	I-pass	0.00	0.00	−0.003	0.06	0.08	−0.22	−0.21	0.19	34.35
			II-pass	0.00	0.00	0.00	0.00	−0.08	−0.18	0.19	−0.26	22.64
		II	I-pass	0.00	0.00	−0.05	0.04	0.22	−0.19	−0.34	0.06	36.82
			II-pass	0.00	0.00	0.00	0.00	0.00	−0.17	0.11	−0.56	26.62

Table 5. Thermodynamic parameters related to the air flowing across the parallel duct of Collector-I.

$\dot{m}$	Parameters	Collector-I		Range of Variation	
		I-Pass	**II-Pass**	**I-Pass**	**II-Pass**
8.10 g·s^{-1}	η_{II}	18.39%	18.15%	7.43–22.25%	3.58–27.26%
	η_{I}	29.52%	19.62%	29.14–30.07%	17.63–22.73%
	Δh	22.94 kJ·kg^{-1}	6.70 kJ·kg^{-1}	9.26–29.50 kJ·kg^{-1}	1.21–11.68 kJ·kg^{-1}
	Δb	0.90 kJ·kg^{-1}	0.57 kJ·kg^{-1}	0.16–1.43 kJ·kg^{-1}	0.04–1.11 kJ·kg^{-1}
	$\dot{S}_{g,p}$	1.69 × 10^{-4} W·K^{-1}	0.01 W·K^{-1}	-	-
	$\dot{S}_g$	0.10 W·K^{-1}	0.07 W·K^{-1}	0.03–0.14 W·K^{-1}	0.02–0.09 W·K^{-1}
	ΔS_{h}	0.07 kJ·kg^{-1}·K^{-1}	0.02 kJ·kg^{-1}·K^{-1}	0.03–0.09 kJ·kg^{-1}·K^{-1}	0.01–0.03 kJ·kg^{-1}·K^{-1}
	Q_{u}	0.22 kW	0.14 kW	0.10–0.26 kW	0.06–0.20 kW
	I	37.83 W	20.40 W	11.35–51.79 W	5.58–28.10 W
10.10 g·s^{-1}	η_{II}	18.94%	19.44%	7.65–23.10%	6.15–25.86%
	η_{I}	31.74%	21.32%	31.24–33.59%	19.13–24.21%
	Δh	18.68 kJ·kg^{-1}	6.52 kJ·kg^{-1}	7.34–23.54 kJ·kg^{-1}	1.40–11.01 kJ·kg^{-1}
	Δb	0.60 kJ·kg^{-1}	0.48 kJ·kg^{-1}	0.11–1.00 kJ·kg^{-1}	0.05–0.90 kJ·kg^{-1}
	$\dot{S}_{g,p}$	3.40 × 10^{-4} W·K^{-1}	0.03 W·K^{-1}	-	-
	$\dot{S}_g$	0.10 W·K^{-1}	0.06 W·K^{-1}	0.02–0.13 W·K^{-1}	0.01–0.09 W·K^{-1}
	ΔS_{h}	0.06 kJ·kg^{-1}·K^{-1}	0.02 kJ·kg^{-1}·K^{-1}	0.02–0.07 kJ·kg^{-1}·K^{-1}	0.00–0.03 kJ·kg^{-1}·K^{-1}
	Q_{u}	0.23 kW	0.16 kW	0.10–0.28 kW	0.06–0.20 kW
	I	28.36	19.80 W	7.95–39.01 W	4.80–27.57 W
12.10 g·s^{-1}	η_{II}	15.47%	18.17%	9.42–19.15%	8.09–24.71%
	η_{I}	34.26%	22.68%	33.79–34.71%	21.20–24.44%
	Δh	16.02 kJ·kg^{-1}	5.72 kJ·kg^{-1}	8.15–20.34 kJ·kg^{-1}	1.81–9.16 kJ·kg^{-1}
	Δb	0.44 kJ·kg^{-1}	0.36 kJ·kg^{-1}	0.12–0.65 kJ·kg^{-1}	0.06–0.64 kJ·kg^{-1}
	$\dot{S}_{g,p}$	6.12 × 10^{-4} W·K^{-1}	0.02 W·K^{-1}	-	-
	$\dot{S}_g$	0.09 W·K^{-1}	0.06 W·K^{-1}	0.02–0.13 W·K^{-1}	0.01–0.08 W·K^{-1}
	ΔS_{h}	0.05 kJ·kg^{-1}·K^{-1}	0.02 kJ·kg^{-1}·K^{-1}	0.02–0.06 kJ·kg^{-1}·K^{-1}	0.00–0.03 kJ·kg^{-1}·K^{-1}
	Q_{u}	0.25 kW	0.17 kW	0.11–0.30 kW	0.07–0.20 kW
	I	28.69 W	19.06 W	7.02–38.86 W	4.32–25.93 W

Table 6. Thermodynamic parameters of the air flowing across the parallel duct of Collector-II.

$\dot{m}$	Parameters	Collector-II		Range of Variation	
		I-Pass	**II-Pass**	**I-Pass**	**II-Pass**
8.10 g·s^{-1}	η_{II}	24.87%	19.80%	11.37–33.59%	6.87–31.42%
	η_{I}	31.46%	19.74%	30.75–31.99%	14.59–24.02%
	Δh	28.21 kJ·kg^{-1}	5.92 kJ·kg^{-1}	12.48–36.55 kJ·kg^{-1}	2.01–7.85 kJ·kg^{-1}
	Δb	1.31 kJ·kg^{-1}	0.58 kJ·kg^{-1}	0.28–2.03 kJ·kg^{-1}	0.10–0.90 kJ·kg^{-1}
	$\dot{S}_{g,p}$	1.70 × 10^{-4} W·K^{-1}	0.02 W·K^{-1}	-	-
	$\dot{S}_g$	0.10 W·K^{-1}	0.06 W·K^{-1}	0.03–0.14 W·K^{-1}	0.01–0.09 W·K^{-1}
	ΔS_{h}	0.10 kJ·kg^{-1}·K^{-1}	0.01 kJ·kg^{-1}·K^{-1}	0.04–0.11 kJ·kg^{-1}·K^{-1}	0.00–0.02 kJ·kg^{-1}·K^{-1}
	Q_{u}	0.23 kW	0.14 kW	0.1–0.28 kW	0.50–0.18 kW
	I	31.50 W	19.85 W	9.04–43.23 W	4.28–27 W
10.10 g·s^{-1}	η_{II}	25.08%	17.62%	14.26–31.51%	5.23–28.61%
	η_{I}	34.63%	23.86%	34.02–36.47%	20.90–27.38%
	Δh	24.58 kJ·kg^{-1}	5.39 kJ·kg^{-1}	10.87–31.11 kJ·kg^{-1}	1.91–7.55 kJ·kg^{-1}
	Δb	1.00 kJ·kg^{-1}	0.47 kJ·kg^{-1}	0.21–1.62 kJ·kg^{-1}	0.10–0.77 kJ·kg^{-1}

Table 6. *Cont.*

$\dot{m}$	Parameters	Collector-II		Range of Variation	
		I-Pass	II-Pass	I-Pass	II-Pass
10.10 g·s^{-1}	$\dot{S}_{g,p}$	3.40×10^{-4} W·K^{-1}	0.03 W·K^{-1}	-	-
	$\dot{S}_g$	0.10 W·K^{-1}	0.07 W·K^{-1}	0.02–0.14 W·K^{-1}	0.01–0.09 W·K^{-1}
	ΔS_h	0.08 kJ·kg^{-1}·K^{-1}	0.01 kJ·kg^{-1}·K^{-1}	0.03–0.10 kJ·kg^{-1}·K^{-1}	0.00–0.02 kJ·kg^{-1}·K^{-1}
	Q_u	0.25 kW	0.18 kW	0.11–0.31 kW	0.07–0.21 kW
	I	29.77 W	20.60 W	8.50–41.03 W	5.44–28.05 W
12.10 g·s^{-1}	η_{II}	22.73%	17.93%	16.00–27.65%	8.71–31.52%
	η_I	36.66%	26.84%	35.97–37.16%	25.00–28.85%
	Δh	21.12 kJ·kg^{-1}	4.72 kJ·kg^{-1}	9.95–27.36 kJ·kg^{-1}	1.81–6.44 kJ·kg^{-1}
	Δb	0.72 kJ·kg^{-1}	0.35 kJ·kg^{-1}	0.17–1.08 kJ·kg^{-1}	0.07–0.54 kJ·kg^{-1}
	$\dot{S}_{g,p}$	6.10×10^{-4} W·K^{-1}	0.02 W·K^{-1}	-	-
	$\dot{S}_g$	0.09 W·K^{-1}	0.07 W·K^{-1}	0.02–0.13 W·K^{-1}	0.01–0.098 W·K^{-1}
	ΔS_h	0.06 kJ·kg^{-1}·K^{-1}	0.01 kJ·kg^{-1}·K^{-1}	0.03–0.10 kJ·kg^{-1}·K^{-1}	0.00–0.2 kJ·kg^{-1}·K^{-1}
	Q_u	0.27 kW	0.20 kW	0.12–0.33 kW	0.08–0.24 kW
	I	28.74	56.05	6.44–40.38 W	4.89–86.15

5. Conclusions

The two-pass solar air collector was statistically, as well as thermodynamically, examined. The LARS algorithm was used to determine whether the polynomial model complies with the experimentally determined energy distribution across the given air passage or not. Some of the relevant points were extracted and enumerated as follows.

1. The useful heat rate unsteadily varied with time as the air flow rate increased inside Collector-I and Collector- II. Relatively, Collector-II will have a higher deviation around its mean than Collector-I. The Q_u distribution function would share the characteristic of the higher-order Gaussian function. A rise of 16.55% and 35.52% in Q_u was, respectively, estimated as the air flow rate changed from 8.10 g·s^{-1} to 12.10 g·s^{-1} for the I and II-passes of Collector-II. Correspondingly, it elevated by 16.32% and 15.88% for I and II-passes of Collector-I.
2. The exergy of the air was dropped by 23.12% (Collector-II (I-pass)) and 34.38% (Collector-I (I-pass)) when the air flow rate increased from 8.10 g·s^{-1} to 10.10 g·s^{-1}, which was further curtailed by 29.46% (Collector-II (I-pass)) and 25.25% (Collector-I (I-pass)) at 12.10 g·s^{-1}. In the case of the II-pass of Collector-I and Collector-II, the fall in the exergy of the air was, respectively, 27% and 17.74% as the air flow rate rose from 10.10 g·s^{-1} to 12.10 g·s^{-1}. The standard deviation in the exergy data-sets for both Collectors-I and II reduced with a rise in the air flow rate. The attaining of the peak value of the exergy gain with time is relatively fast in Collector-I as compared to Collector-II. The least angle regression showed that the variation in exergy model with time for Collector-I would possess a higher degree of oscillation than the corresponding model derived for Collector-II.
3. As the air flow rate surged to 10.10 g·s^{-1}, the second law efficiency of the air was marginally increased by 0.85% and dropped by 11.05% for I and II-passes of Collector-II, respectively. In the same manner, it was, correspondingly, increased by 3.86% and 1.08% for the I and II-passes of Collector-I. The further rise in the air flow rate up to 12.10 g·s^{-1} caused the second law efficiency to be dropped by 18.27% (I-pass) and 5.68% (II-pass) for Collector-I. Conversely, it was curtailed by 9.37% for I-pass and slightly increased by 1.78% for II-pass of Collector-II. The polynomial equation fitting η_{II} for Collector-II has high dimensionality as compared to the equation derived for η_{II} of Collector-I. The first law efficiency for the Collector-I was enhanced by 16.06% (I-pass) and 15.63% (II-pass) as the air flow rate rose to 12.10 g·s^{-1}. In case of Collector-II,

η_I was elevated by 16.53% (I-pass) and 35.94% (II-pass) at the same air flow rate. The LARS models for η_I of Collectors-I and II do not have much perturbation with time

4. Entropy generation in Collector-II was double, in magnitude, the corresponding value derived for Collector-I. From an exergy perspective, it was assessed that the two-pass flow system would not be beneficial for the low air flow rate. The rise in the air flow rate would cause higher exergy loss for I-pass of Collectors I and II, whereas it would be relatively low in the II-pass. Comparatively, the Collector-II is a better option to exploit the maximum available energy from the carrier fluid.

Supplementary Materials: The following supporting information can be downloaded at: https://www.mdpi.com/article/10.3390/en16052461/s1, Table S1: Uncertainty in the experimental measurement.

Funding: This research received no external funding.

Data Availability Statement: Not applicable.

Conflicts of Interest: The authors declare no conflict of interest.

Nomenclature

ψ	Exergy function for the given system	kJ·kg^{-1}
η_I	First law efficiency of the carrier fluid	%
η_{II}	Second law efficiency of the carrier fluid	%
Γ	A set of the coefficient vectors	-
β	The angle formed by the estimated response with a correlated predictor	°
ϕ	A set of active variables that are highly correlated with the residual	-
ξ	Optimal step size	
$\hat{\psi}$	Prediction vector of exergy	kJ·kg^{-1}
u_2	Unit vector lying along the bisector	
Δh	The change in the enthalpy of the air	kJ·kg^{-1}
Δb	The change in the Keenan function	kJ·kg^{-1}
T	Temperature	K
A_{min}	The minimum exergy intake to perform work	kJ·kg^{-1}
A	The actual exergy required to carry out a task	kJ·kg^{-1}
ΔP	Pressure-drop along the length of the collector	N·m^{-2}
P	Pressure at the inlet of the collector	N·m^{-2}
t	Time duration	s
$\dot{S}_g$	Exergy generation due to internal irreversibility	W·K^{-1}
$\dot{S}_{g,p}$	Exergy generation due to air friction	W·K^{-1}
$\dot{m}$	The air flow rate across passage of the Solar air collector	g·s^{-1}
Q_u	The useful heat gain rate by the air (system)	kW
Q_r	The rate of heat transfer from the reservoir	kW
$\dot{Q}$	The heat transfer rate to the system	kW
ΔS_h	Entropy transfer with heat	kW·kg^{-1}/K
p	Coefficient of the polynomial model	-
n	Order of polynomial equation	-
T_{fi}	The carrier fluid temperature at the inlet of the collector	K
T_a	The ambient or reference temperature for the analysis	K
I	The rate of exergy destruction in the system	W

References

1. IEA. *Renewable Electricity Growth is Accelerating Faster Than Ever Worldwide, Supporting the Emergence of the New Global Energy Economy. Analysis and Forecasts to 2026*; IEA: Paris, France, 2021. Available online: https://www.iea.org/news/renewable-electricity-growth-is-accelerating-faster-than-ever-worldwide-supporting-the-emergence-of-the-new-global-energy-economy (accessed on 16 September 2022).
2. Grand View Research Inc. *Solar Thermal Collectors Market Size, Share & Trends Analysis Report by Product (Concen-trating, Non-Concentrating (Flat Plate, Evacuated Tube, Unglazed Water Collector, Air Collector), By Application, By Region, And Segment Forecasts, 2018–2025 (Report no. GVR-1-68038-690-5)*; Grand View Research Inc.: Dublin, Ireland, 2017; Available online: https://www.grandviewresearch.com/industry-analysis/solar-thermal-collector-market (accessed on 16 September 2022).

3. Dhaundiyal, A. Developing a Grey Forecasting Model for the Air Flowing across the Parallel Plate Duct. *Energies* **2022**, *15*, 5562. [CrossRef]
4. Dhaundiyal, A.; Gebremicheal, G.H. The Stack Effect on the Thermal-Fluid Behaviour of a Solar Collector. *Energies* **2022**, *15*, 1188. [CrossRef]
5. Reddy, J.; Jagadish; Negi, S.; Das, B.; Ehyaei, M.A.; Assad, M.E.H. Energy and exergy analysis of a trapezoidal absorber plate-based solar air collector. *Energy Sci. Eng.* **2022**, *10*, 1067–1082. [CrossRef]
6. Khalil, W.; Obaid, Z.A.H.; Dawood, H.K. Exergy analysis of single-flow solar air collectors with different configurations of absorber plates. *Heat Transf. Asian Res.* **2019**, *48*, 3600–3616. [CrossRef]
7. Dhaundiyal, A.; Gebremicheal, G.H. The effect of psychrometry on the performance of a solar collector. *Environ. Sci. Pollut. Res.* **2022**, *29*, 13445–13458. [CrossRef]
8. Pathak, P.K.; Chandra, P.; Raj, G. Energy and exergy analysis of corrugated plate solar collector by forced convection using two different absorber plate material. *Heat Mass Transf.* **2021**, *57*, 565–581. [CrossRef]
9. Said, Z.; A.Alim, M.; Janajreh, I. Exergy efficiency analysis of a flat plate solar collector using graphene based nanofluid. *IOP Conf. Series Mater. Sci. Eng.* **2015**, *92*, 012015. [CrossRef]
10. Ashouri, M.; Ahmadi, M.H.; Feidt, M.; Astaraei, F.R. Exergy and energy analysis of a regenerative organic Rankine cycle based on flat plate solar collectors. *Mech. Ind.* **2017**, *18*, 217. [CrossRef]
11. Rostami, S.; Sepehrirad, M.; Dezfulizadeh, A.; Hussein, A.K.; Goldanlou, A.S.; Shadloo, M.S. Exergy Optimization of a Solar Collector in Flat Plate Shape Equipped with Elliptical Pipes Filled with Turbulent Nanofluid Flow: A Study for Thermal Management. *Water* **2020**, *12*, 2294. [CrossRef]
12. Lakshmipathy, B.; Sivakumar, K.; Senthilkumar, M.; Kajavali, A.; Singh, S.C.E.; Murugan, S. Performance Characterization of a Solar Cavity Collector Using Artificial Neural Network. *Model. Simul. Eng.* **2022**, *2022*, 1–9. [CrossRef]
13. El-Sebaii, A.; Aboul-Enein, S.; Ramadan, M.; Shalaby, S.; Moharram, B. Investigation of thermal performance of-double pass-flat and v-corrugated plate solar air heaters. *Energy* **2011**, *36*, 1076–1086. [CrossRef]
14. Boulemtafes-Boukadoum, A.; Benzaoui, A. CFD based Analysis of Heat Transfer Enhancement in Solar Air Heater Provided with Transverse Rectangular Ribs. *Energy Procedia* **2014**, *50*, 761–772. [CrossRef]
15. Aissaoui, F.; Benmachiche, A.; Brima, A.; Belloufi, D.; Bahloul, D.; Belloufi, Y. Experimental and Theoretical Analysis on Thermal Performance of the Flat Plate Solar Air Collector. *Int. J. Heat Technol.* **2016**, *34*, 213–220. [CrossRef]
16. Velmurugan, P.; Kalaivanan, R. Energy and exergy analysis in double-pass solar air heater. *Sadhana—Acad. Proc. Eng. Sci.* **2016**, *41*, 369–376. [CrossRef]
17. Velmurugan, P.; Kalaivanan, R. Energy and Exergy Analysis of Multi-Pass Flat Plate Solar Air Heater—An Analytical Approach. *Int. J. Green Energy* **2015**, *12*, 810–820. [CrossRef]
18. Sandali, M.; Boubekri, A.; Benhamza, A.; Settou, B.; Halassa, D.; Mennouche, D. A simulation study of a solar collector using phase change materials for air heating application needs. *AIP Conf. Proc.* **2017**, *1814*, 020010. [CrossRef]
19. El-Said, E.M. Numerical investigations of fluid flow and heat transfer characteristics in solar air collector with curved perforated baffles. *Eng. Rep.* **2020**, *2*, e12142. [CrossRef]
20. Kalbande, V.P.; Walke, P.V.; Shelke, R. Aluminum-based thermal storage system with solar collector using nanofluid. *Energy Storage* **2019**, *1*, e99. [CrossRef]
21. Zheng, X.; Shi, R.; Wang, Y.; You, S.; Zhang, H.; Xia, J.; Wei, S. Mathematical modeling and performance analysis of an integrated solar heating and cooling system driven by parabolic trough collector and double-effect absorption chiller. *Energy Build.* **2019**, *202*, 109400. [CrossRef]
22. Gopi, G.; Premalatha, M.; Arthanareeswaran, G. Transient mathematical modelling and investigation of radiation and design parameters on the performance of multi-effect solar still integrated with evacuated tube collector. *Energy Convers. Manag. X* **2022**, *14*, 100210. [CrossRef]
23. Zima, W.; Cebula, A.; Cisek, P. Mathematical Model of a Sun-Tracked Parabolic Trough Collector and Its Verification. *Energies* **2020**, *13*, 4168. [CrossRef]
24. Ding, D.; He, W.; Liu, C. Mathematical Modeling and Optimization of Vanadium-Titanium Black Ceramic Solar Collectors. *Energies* **2021**, *14*, 618. [CrossRef]